Bridging electromagnetic and carrier transport calculations for three-dimensional modelling of plasmonic solar cells

Xiaofeng Li,* Nicholas P. Hylton, Vincenzo Giannini, Kan-Hua Lee, Ned J. Ekins-Daukes, and Stefan A. Maier

Blackett Laboratory, Department of Physics, Imperial College London, London SW7 2AZ, UK
**xfl_79@yahoo.com.cn*

Abstract: We report three-dimensional modelling of plasmonic solar cells in which electromagnetic simulation is directly linked to carrier transport calculations. To date, descriptions of plasmonic solar cells have only involved electromagnetic modelling without realistic assumptions about carrier transport, and we found that this leads to considerable discrepancies in behaviour particularly for devices based on materials with low carrier mobility. Enhanced light absorption and improved electronic response arising from plasmonic nanoparticle arrays on the solar cell surface are observed, in good agreement with previous experiments. The complete three-dimensional modelling provides a means to design plasmonic solar cells accurately with a thorough understanding of the plasmonic interaction with a photovoltaic device.

OCIS codes: (040.5350) Photovoltaic; (240.6680) Surface plasmon; (290.1990) Diffusion.

References and links

1. H. A. Atwater, and A. Polman, "Plasmonics for improved photovoltaic devices," Nat. Mater. **9**(3), 205–213 (2010).
2. K. R. Catchpole, and A. Polman, "Plasmonic solar cells," Opt. Express **16**(26), 21793–21800 (2008).
3. V. Giannini, A. I. Fernández-Domínguez, Y. Sonnefraud, T. Roschuk, R. Fernández-García, and S. A. Maier, "Controlling light localization and light-matter interactions with nanoplasmonics," Small **6**(22), 2498–2507 (2010).
4. V. E. Ferry, J. N. Munday, and H. A. Atwater, "Design considerations for plasmonic photovoltaics," Adv. Mater. **22**(43), 4794–4808 (2010).
5. S. A. Maier, M. L. Brongersma, P. G. Kik, S. Meltzer, A. A. G. Requicha, and H. A. Atwater, "Plasmonics – a route to nanoscale optical devices," Adv. Mater. **13**(19), 1501–1505 (2001).
6. S. A. Maier, *Plasmonics: Fundamentals and Applications* (Springer, 2007).
7. E. M. Hicks, S. Zou, G. C. Schatz, K. G. Spears, R. P. Van Duyne, L. Gunnarsson, T. Rindzevicius, B. Kasemo, and M. Käll, "Controlling plasmon line shapes through diffractive coupling in linear arrays of cylindrical nanoparticles fabricated by electron beam lithography," Nano Lett. **5**(6), 1065–1070 (2005).
8. T. Shegai, V. D. Miljković, K. Bao, H. Xu, P. Nordlander, P. Johansson, and M. Käll, "Unidirectional broadband light emission from supported plasmonic nanowires," Nano Lett. **11**(2), 706–711 (2011).
9. F. J. Beck, S. Mokkapati, A. Polman, and K. R. Catchpole, "Asymmetry in photocurrent enhancement by plasmonic nanoparticle arrays located on the front or on the rear of solar cells," Appl. Phys. Lett. **96**(3), 033113 (2010).
10. S. Pillai, K. R. Catchpole, T. Trupke, and M. A. Green, "Surface plasmon enhanced silicon solar cells," J. Appl. Phys. **101**(9), 093105 (2007).
11. P. Matheu, S. H. Lim, D. Derkacs, C. McPheeters, and E. T. Yu, "Metal and dielectric nanoparticle scattering for improved optical absorption in photovoltaic devices," Appl. Phys. Lett. **93**(11), 113108 (2008).
12. K. Nakayama, K. Tanabe, and H. A. Atwater, "Plasmonic nanoparticle enhanced light absorption in GaAs solar cells," Appl. Phys. Lett. **93**(12), 121904 (2008).
13. X. H. Chen, C. C. Zhao, L. Rothberg, and M. K. Ng, "Plasmon enhancement of bulk heterojunction organic photovoltaic devices by electrode modification," Appl. Phys. Lett. **93**(12), 123302 (2008).
14. O. Stenzel, A. Stendal, K. Voigtsberger, and C. von Borczyskowski, "Enhancement of the photovoltaic conversion efficiency of copper phthalocyanine thin film devices by incorporation of metal clusters," Sol. Energy Mater. Sol. Cells **37**(3-4), 337–348 (1995).
15. T. L. Temple, G. D. K. Mahanama, H. S. Reehal, and D. M. Bagnall, "Influence of localized surface plasmon excitation in silver nanoparticles on the performance of silicon solar cells," Sol. Energy Mater. Sol. Cells **93**(11),

#145911 - $15.00 USD Received 13 Apr 2011; revised 11 May 2011; accepted 13 May 2011; published 30 Jun 2011

1978–1985 (2009).
16. P. Spinelli, M. Hebbink, R. de Waele, L. Black, F. Lenzmann, and A. Polman, "Optical impedance matching using coupled plasmonic nanoparticle arrays," Nano Lett. **11**(4), 1760–1765 (2011).
17. J. R. Nagel, and M. A. Scarpulla, "Enhanced absorption in optically thin solar cells by scattering from embedded dielectric nanoparticles," Opt. Express **18**(Suppl 2), A139–A146 (2010).
18. R. A. Pala, J. White, E. Barnard, J. Liu, and M. L. Brongersma, "Design of plasmonic thin-film solar cells with broadband absorption enhancements," Adv. Mater. **21**(34), 3504–3509 (2009).
19. W. Wang, S. M. Wu, K. Reinhardt, Y. L. Lu, and S. C. Chen, "Broadband light absorption enhancement in thin-film silicon solar cells," Nano Lett. **10**(6), 2012–2018 (2010).
20. C. Hägglund, S. P. Apell, and B. Kasemo, "Maximized optical absorption in ultrathin films and its application to plasmon-based two-dimensional photovoltaics," Nano Lett. **10**(8), 3135–3141 (2010).
21. J. N. Munday, and H. A. Atwater, "Large integrated absorption enhancement in plasmonic solar cells by combining metallic gratings and antireflection coatings," Nano Lett., (2010), http://dx.doi.org/10.1021/nl101875t.
22. S. Mokkapati, F. J. Beck, A. Polman, and K. R. Catchpole, "Designing periodic arrays of metal nanoparticles for light-trapping applications in solar cells," Appl. Phys. Lett. **95**(5), 053115 (2009).
23. J. R. Cole, and N. J. Halas, "Optimized plasmonic nanoparticle distributions for solar spectrum harvesting," Appl. Phys. Lett. **89**(15), 153120 (2006).
24. M. D. Kelzenberg, S. W. Boettcher, J. A. Petykiewicz, D. B. Turner-Evans, M. C. Putnam, E. L. Warren, J. M. Spurgeon, R. M. Briggs, N. S. Lewis, and H. A. Atwater, "Enhanced absorption and carrier collection in Si wire arrays for photovoltaic applications," Nat. Mater. **9**(3), 239–244 (2010).
25. F. J. Beck, A. Polman, and K. R. Catchpole, "Tunable light trapping for solar cells using localized surface plasmons," J. Appl. Phys. **105**(11), 114310 (2009).
26. J. Nelson, *The Physics of Solar Cells* (Imperial College Press, 2003).
27. Comsol Multiphysics, *http://www.comsol.com/*
28. G. A. Swartz, "Computer model of amorphous silicon solar cell," J. Appl. Phys. **53**(1), 712–719 (1982).
29. J. R. Lowney, and H. S. Bennett, "Majority and minority electron and hole mobilities in heavily doped GaAs," J. Appl. Phys. **69**(10), 7102–7110 (1991).
30. H. S. Bennett, "Majority and minority electron and hole mobilities in heavily doped gallium aluminum arsenide," J. Appl. Phys. **80**(7), 3844–3853 (1996).
31. D. E. Aspnes, S. M. Kelso, R. A. Logan, and R. Bhat, "Optical properties of Al_xGa_{1-x} As," J. Appl. Phys. **60**(2), 754–767 (1986).
32. E. D. Palik, *Handbook of Optical Constants of Solids*, (Academic Press, 1985).
33. S. H. Lim, W. Mar, P. Matheu, D. Derkacs, and E. T. Yu, "Photocurrent spectroscopy of optical absorption enhancement in silicon photodiodes via scattering from surface plasmon polaritons in gold nanoparticles," J. Appl. Phys. **101**(10), 104309 (2007).
34. F. J. Beck, E. Verhagen, S. Mokkapati, A. Polman, and K. R. Catchpole, "Resonant SPP modes supported by discrete metal nanoparticles on high-index substrates," Opt. Express **19**(Suppl 2), A146–A156 (2011).
35. G. W. Shu, W. C. Liao, C. L. Hsu, J. Y. Lee, I. J. Hsu, J. L. Shen, M. D. Yang, C. H. Wu, Y. C. Lee, and W. C. Chou, "Enhanced conversion efficiency of GaAs solar cells using Ag nanoparticles," Adv. Sci. Lett. **3**, 368–372 (2010).
36. J. Meier, J. Spitznagel, U. Kroll, C. Bucher, S. Fay, T. Moriarty, and A. Shah, "Potential of amorphous and microcrystalline silicon solar cells," Thin Solid Films **451–452**, 518–524 (2004).
37. A. J. Huber, F. Keilmann, J. Wittborn, J. Aizpurua, and R. Hillenbrand, "Terahertz near-field nanoscopy of mobile carriers in single semiconductor nanodevices," Nano Lett. **8**(11), 3766–3770 (2008).

1. Introduction

The application of surface plasmons (SPs) in photovoltaic devices has recently attracted considerable attention due to potential improvements to device absorption without increasing the physical thickness of the photoactive medium [1–8]. Performance improvement has been predicted through simulations and verified in experiments for solar cells (SCs) based on both inorganic and organic materials [9–15] with properly designed plasmonic nanostructures [16–25]. In order to comprehensively evaluate a SC, several crucial device parameters, e.g., short-circuit photocurrent density (J_{sc}), current-voltage (I-V) curve, fill factor (*FF*), light-conversion efficiency (η), *etc.* are required. These parameters can be readily achieved in photovoltaic experiments [4,10,12,25]; however, most previous simulations of plasmonic SCs (PSCs) consider only the optical absorption through solving Maxwell's equations. Although improved photocurrent has been predicted in several articles [17,21], ideal carrier transport (ICT) was assumed, namely that each photo-generated electron-hole pair can successfully contribute to the photocurrent. Under this condition the realistic solar cell behaviour and configuration (*e.g.*, doping profile, carrier mobility, carrier loss, *etc.*) are ignored. However, this approach is not always accurate since in a real SC the photo-generated carriers will recombine (prior to collection) under various loss mechanisms, such as surface and bulk carrier recombination or

#145911 - $15.00 USD Received 13 Apr 2011; revised 11 May 2011; accepted 13 May 2011; published 30 Jun 2011

short carrier diffusion [26]. The device performance is overestimated especially for those SCs based on materials with low carrier mobility and short carrier lifetime, *e.g.*, hydrogenated amorphous silicon (α-Si:H). Hence, the exact electronic response must be considered in order to obtain accurate I-V characteristics for a complete evaluation of the SCs. Therefore, an accurate model of PSCs must consider both the electromagnetic (light absorption) and electronic (carrier transport) properties together in a single simulation. Due to the strongly localized confinement of SP waves, such work has to be performed in both frequency and all spatial domains.

This paper presents exact three-dimensional (3D) simulations of PSCs that link both optical absorption and carrier transport together. We have verified the need to perform the full calculation of the electronic response of a SC by comparing the results of gallium arsenide (GaAs) and a-Si:H SCs under a purely electromagnetic treatment and using our full calculation. External quantum efficiency (EQE) and I-V characteristics before and after plasmonic design were then calculated, in order to obtain complete information about the performance improvement of SCs (*e.g.*, J_{sc}, *FF*, η, *etc*). Finally, the spatial distributions of power flow and carrier concentration profiles were extracted from the simulation.

2. Theory

Our work aims to realize a modular 2-step 3D simulation based on the finite element method [27]. The first step is to perform an exact electromagnetic calculation (inherent in which are all optical mechanisms, including any shading effect due to metallic nanoparticles on the surface) based on 3D Maxwell's equations in the frequency domain. A single unit cell was used in conjunction with periodic Floquet-Bloch boundaries to represent the whole structure, and the standard AM1.5G spectrum was introduced as the incident light source. Linearly polarized light was used since the device is rotationally symmetric and insensitive to the light polarization. The photo-generation rate extracted from the optical calculation is also used for the exact carrier transport calculation in the second step, which is based on two sub-modules simulating electron and hole transports, respectively, and one sub-module for electrostatic potential (see the supplemental material). The 3D transport equations were solved under solar injection and forward electric bias for the calculation of photocurrent and dark current. Finally, information on SC performance, including EQE, J_{sc}, I-V curve, open-circuit voltage (V_{oc}), maximum output power density (P_{max}), *FF*, η, *etc*. can all be obtained for the optimisation of PSC designs.

The electronic response of solar cells (SCs) can be simulated accurately using three-dimensional (3D) transport equations for electrons and holes. In order to develop a general model capable of simulating various SCs, including those based on heterojunctions, discontinuity of the intrinsic material parameters at heterojunction interfaces must be taken into account. The simulation of homojunction SCs is then a specific case where the discontinuity term is removed from the carrier transport equations. The generalized 3D carrier transport equations (in steady state) used in our model are [26]

$$\nabla\left[-D_n\nabla n + n\mu_n\left(\nabla\Phi + \frac{\nabla\chi}{q} + \frac{k_BT}{q}\nabla\ln N_c\right)\right] = g(x,y,z,\lambda) - U, \qquad (1)$$

$$\nabla\left[-D_p\nabla p - p\mu_p\left(\nabla\Phi + \frac{\nabla\chi}{q} + \frac{\nabla E_g}{q} - \frac{k_BT}{q}\nabla\ln N_v\right)\right] = g(x,y,z,\lambda) - U, \qquad (2)$$

where n (p) is the electron (hole) concentration, $D_n = \mu_n K_B T/q$ ($D_p = \mu_p K_B T/q$) is the electron (hole) diffusion coefficient, μ_n (μ_p) is the electron (hole) mobility, K_B is Boltzmann's constant, T (= 300 K) is the operating temperature, q is the electron charge, Φ is the electrostatic potential, χ is the electron affinity, E_g is the material band gap, N_c (N_v) is the effective conduction (valence) band density of states, $g(x, y, z, \lambda) = \alpha(x, y, z, \lambda)P_s(x, y, z, \lambda)$ is the generation rate, α is the material absorption coefficient, P_s is the power flux calculated

#145911 - $15.00 USD Received 13 Apr 2011; revised 11 May 2011; accepted 13 May 2011; published 30 Jun 2011

from the electromagnetic model, and U is the rate of carrier loss due to Shockley-Read-Hall, radiative, and Auger recombination.

The electrostatic potential Φ is determined by the charge profiles in the device according to the 3D Poisson's equation

$$\nabla^2\Phi = \frac{q}{\varepsilon}(n - p - C), \tag{3}$$

where ε is the material permittivity, $C = N_d - N_a$ is the impurity concentration defined as the sum of the concentrations of the ionized donors N_d and acceptors N_a, including the signs of the compensated charges.

The calculated spatial profiles of n and p are used to compute the frequency-dependent photocurrent for electrons and holes, respectively [*i.e.*, $j_n(x,y,z,\lambda) = qD_n\nabla n$ and $j_p(x,y,z,\lambda) = -qD_p\nabla p$]. The corresponding short-circuit current density $j_{sc}(\lambda)$ is then given by the averaged photocurrent at the surface of the SCs

$$j_{sc}(\lambda) = \frac{1}{\Lambda^2}\int_{-\Lambda/2}^{\Lambda/2}\int_{-\Lambda/2}^{\Lambda/2}\left|j_n(x,y,L,\lambda) + j_p(x,y,L,\lambda)\right|dxdy, \tag{4}$$

where L is the total thickness of the photoactive layers. The external quantum efficiency (EQE) is then obtained by using $\mathrm{EQE}(\lambda) = j_{sc}(\lambda)/[qb_s(\lambda)]$, where b_s is the solar incident flux. The overall short-circuit current density J_{sc} can then be expressed by $J_{sc} = \int j_{sc}(\lambda)\mathrm{d}\lambda$.

Considering dark current $J_d(V)$ and device resistances, the current-voltage (I-V) relation is written as

$$J(V) = J_{sc} - J_d(V) - \frac{V + J(V)R_s}{R_{sh}}, \tag{5}$$

where R_s and R_{sh} are series and shunt resistances, respectively, and $J_d(V)$ is obtained by applying forward electric bias into Eqs. (1) and (2), neglecting the generation terms. From the I-V curve, parameters including open-circuit voltage V_{oc}, maximum output power density P_{max}, fill factor [$FF = P_{max}/(J_{sc}V_{oc})$], and light-conversion efficiency ($\eta = P_{max}/P_{sun}$, where P_{sun} is the overall incident light power density) can be obtained.

3. Simulation results

Table 1. Key Parameters Used in the Simulation [23,25–29].

	Layers	Doping (cm^{-3})	μ_n (cm^2/Vs)	μ_p (cm^2/Vs)	τ_n	τ_p
GaAs SCs	window	1×10^{18}	100	10	1 ps	10 ns
	emitter	4×10^{18}	1100	80	1 ns	10 ns
	base	2×10^{17}	4000	80	1 ns	10 ns
	BSF	2×10^{18}	100	10	1 ns	1 ps
α-Si:H SCs	p region	1.3×10^{17}	4.6×10^{-2}	0.5	2 μs	0.34 μs
	i region		4.6×10^{-2}	9.2×10^{-3}	2 μs	2 μs
	n region	4.3×10^{16}	1	9.2×10^{-3}	1.7 μs	2 μs

BSF: back surface field. The doping concentration shown here for α-Si:H SCs is the ionised donor/acceptor concentration; actual dopant levels can be much higher.

Listed in Table 1 [26,28–32] are the key parameters employed in the carrier transport calculations. Additionally, the surface recombination coefficients for minority electrons and holes are taken to be 1×10^6 (1×10^4) cm/s for GaAs (α-Si:H) SCs. Typical non-plasmonic GaAs- and α-Si:H-based SCs [shown in Figs. 1(a) and 1(b) respectively] were first studied to validate the necessity of performing the complete electronic calculation for a real SC. We consider these two types of SCs since they are based on direct-band photoactive materials with typically high and low carrier mobility, respectively, and can therefore test the two

#145911 - $15.00 USD Received 13 Apr 2011; revised 11 May 2011; accepted 13 May 2011; published 30 Jun 2011

modelling treatments under different conditions. Moreover, the large absorption coefficients of the materials make them well-suited to thin-film PSC applications.

Simulation results are displayed in Figs. 1(c) – 1(f), where the results for "full model" originate from the complete 3D calculation, while those for ICT were predicted by spatially integrating and surface-averaging the carrier generation rate (multiplied by electron charge) obtained from the optical calculation. Both current density and EQE of the SCs under solar illumination were analyzed and a discrepancy between the estimation limited to electromagnetic modelling and complete device modelling was observed. This discrepancy relates to the device's internal quantum efficiency (IQE), which can be directly approximated by the ratio of the photocurrents derived from the exact calculation and the assumption of ICT. For GaAs SCs, photocurrent and EQE are overestimated in the short-wavelength part of the spectrum [Fig. 1(e)], while for α-Si:H SCs distinct overestimation was found over a much broader spectral range [Fig. 1(f)]. We believe that the photocurrent decrease in real GaAs SCs (compared to that estimated optically) primarily originates from surface recombination, which is more pronounced at short wavelengths where the absorption coefficient increases dramatically and a large fraction of the incident light is absorbed close to the surface. However, α-Si:H SCs suffer from carrier loss due not only to recombination in the thin emitter (including) but also very low carrier mobility. The latter occurs over a broad spectral range, leading to a low IQE across much of the absorption spectrum. According to our calculation, the exact value of J_{sc} under complete 3D calculation is 17.16 (9.15) mA/cm^2 for the GaAs (α-Si:H) SCs and that estimated from optical calculation is 17.93 (10.88) mA/cm^2. The overestimated value is noticeable and impacts the PSC design (discussed later). It should be noted that the accuracy of pure optical treatment strongly depends on the device configuration; therefore, a robust model simulating both optical and electronic response is necessary.

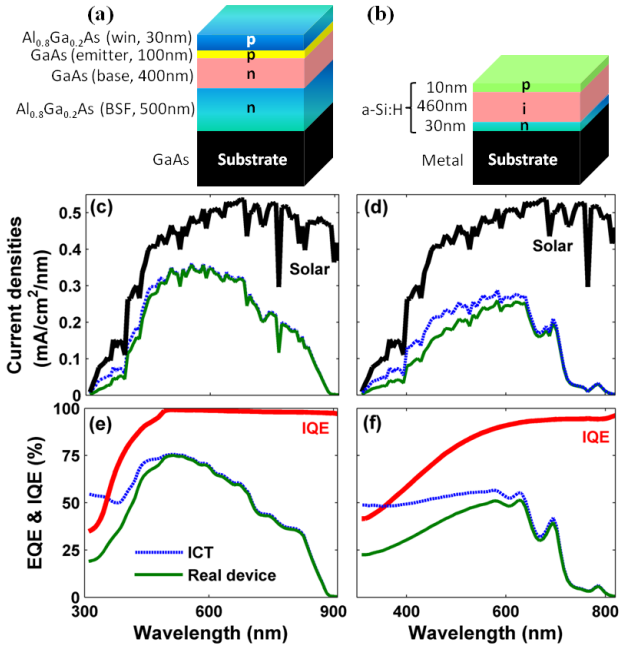

Fig. 1. (a) and (b): schematic diagrams of the considered GaAs- and α-Si:H SCs; (c) and (d): current densities from solar incidence and those generated from the SCs; (e) and (f): EQE and IQE response of the SCs. (a), (c) and (e) [(b), (d) and (f)] are for GaAs (α-Si:H) SCs. The results obtained under ICT assumption are plotted with dashed curves. The observed peaks between 550 nm and 800 nm for α-Si:H SCs are due to Fabry-Perot interference in the cavity.

#145911 - $15.00 USD Received 13 Apr 2011; revised 11 May 2011; accepted 13 May 2011; published 30 Jun 2011

Plasmonic effects can also be incorporated into our model for the simulation of PSC structures [see Figs. 2(a) and 2(b)]. As an example, SCs were simulated with periodic arrays of silver nanoparticles (with a diameter of 160 nm and 400 nm period) on the top surface. The effect of plasmonic design on EQE response is displayed in Figs. 2(c) and 2(d), where both EQE (*i.e.*, photocurrent) degradation and enhancement can be observed. This is a typical feature as reported in previous PSC experiments [12,25,33]. EQE decrease/increase in PSCs was believed to be the result of the destructive/constructive interference between the scattered field from the nanoparticles and that transmitted directly from the incidence, occurring on the blue/red sides of the plasmonic resonance [33]. Alternatively, a recent explanation for this phenomenon suggests that the photocurrent decrease at short wavelengths is due to the resonant modes at the top of the particles, while the enhancement at long wavelengths is from the modes localized at the Ag/substrate interface [34]. We have indeed observed similar behaviour (not shown here) by checking the electric field distribution calculated from our model. Note also that the spectra in Figs. 2(c) and 2(d) exhibit a sharp feature at a wavelength of 400 nm, which is due to the first diffracted order arising from the periodicity of the nanoparticles.

Under the proposed plasmonic design EQE enhancement was realized when $\lambda > 455$ nm (447 nm) for GaAs (α-Si:H) PSCs, benefiting from the preferentially forward light scattering and strong near-field confinement of SPs [1–4]. The plasmonic effect can be controlled effectively by tuning the resonance of a single particle and the coupling strength of the nanoparticles; therefore, the performance of PSCs can be optimized. On the other hand, without considering carrier transport, as shown in Fig. 2, EQE is overestimated and the critical wavelength distinguishing the photocurrent loss and gain regions is blue-shifted.

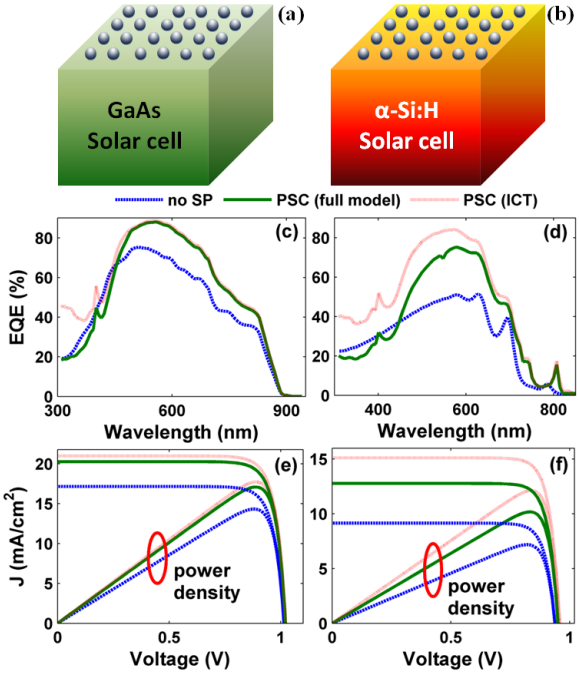

Fig. 2. Schematic diagram (a) [(b)], EQE response (c) [(d)] and I-V curves (e) [(f)] of GaAs [α-Si:H] SCs before (dashed) and after (solid) the proposed plasmonic design with 160nm-diameter silver particles under period of 400 nm. Solid and dot curves are from complete calculation and optical estimation under ICT assumption, respectively. Power densities are also plotted in (e) and (f) so that the detailed information about J_{sc}, V_{oc}, P_{max}, FF, and η can be obtained. The performance enhancement is observed from these figures and the extracted performance parameters are listed in Table 2.

#145911 - $15.00 USD Received 13 Apr 2011; revised 11 May 2011; accepted 13 May 2011; published 30 Jun 2011

In order to acquire the I-V information, the carrier transport module is used again to calculate the dark current response of the SCs under forwardly applied voltages. This was realized in our model by controlling the boundary conditions of the electrostatic potential sub-module [26]; the results are plotted in Figs. 2(e) and 2(f), respectively. In addition, output power densities have also been plotted so that P_{max}, FF, and η could be determined. From these figures, the device performance parameters under various conditions were extracted and listed in Table 2, which shows that, with the incorporation of plasmonic nanostructures, improvement ratios in J_{sc}, P_{max}, and η of more than 18% for GaAs SCs and over 40% for α-Si:H SCs could be achieved. As expected, over-predicted performance under ICT assumption was observed. The difference between these two methods is especially distinct for α-Si:H SCs as shown in Fig. 2(f) and Table 2.

Table 2. Performance Comparison under Various System Configurations

		J_{sc} (mA/cm^2)	V_{oc} (V)	P_{max} (mW/cm^2)	FF	η
GaAs SCs	no SP	17.16	1.028	14.34	81.3%	14.9%
	PSC (full model)	20.28	1.034	17.10	81.6%	17.8%
	(enhancement, %)	(18.2%)	(0.58%)	(19.3%)	(0.37%)	(19.5%)
	PSC (ICT)	21.00	1.035	17.73	81.6%	18.4%
	(enhancement, %)	(22.4%)	(0.68%)	(23.6%)	(0.37%)	(23.5%)
α-Si:H SCs	no SP	9.15	0.94	7.18	83.5%	7.5%
	PSC (full model)	12.78	0.95	10.20	84.0%	10.6%
	(enhancement, %)	(39.7%)	(1.1%)	(42.1%)	(0.6%)	(41.3%)
	PSC (ICT)	15.12	0.96	12.14	83.6%	12.16%
	(enhancement, %)	(65.3%)	(2.1%)	(69.1%)	(0.12%)	(68.0%)

However, neither V_{oc} nor FF exhibit noticeable increases [11,35]. Note that the FF shown here is relatively high, since ideal series (*i.e.*, 0 Ωcm^2) and shunt resistances (*i.e.*, ∞ Ωcm^2) were used for simplicity. Realistic resistance values could be easily integrated into our model [see Eq. (5)], resulting in a more credible FF. Note also that the incorporation of metallic components on the incident surface may lead to an associated reduction in resistance, hence increasing the FF [12,26]. This effect can be included by using appropriate device resistances that reflect the effect of a metallic nanoparticle coating. We also emphasize that the scope of our work is to obtain a full 3D model that considers both the electromagnetic and carrier transport response, and that the optimization of PSCs is beyond the scope of this paper; hence the device performance shown herein may not be maximized compared to some previous reports (*e.g.*, for α-Si:H SCs reported in [36]).

We would like to indicate that there also exists a compromise between a full 3D model and the ICT case by using only low-dimensional electronic model, *i.e.*, based on the assumption that the IQE of the original SC shows no noticeable change after the introduction of plasmonic nanoparticles. In this compromise the original IQE from a 1D electronic calculation and the field profile of the PSCs from our 3D electromagnetic calculation are used to predict the final electronic output. Using this method, J_{sc} values for the considered GaAs and α-Si:H PSCs were recalculated and found to be 20.25 and 13.00 mA/cm^2, respectively, showing an obvious improvement from the ICT case. However, it is unclear if such a compromise remains valid for all cases (different materials and system setups or strong plasmonic effects). For example, if the solar cells are under multi-sun illumination or a higher nanoparticle concentration is employed, the carrier profiles will be modified more strongly by plasmonic design leading to significant modification of the IQE. Furthermore, obtaining detailed spatial information of the electronic parameters is also an important issue, which can only be obtained from a complete 3D simulation.

Therefore, we now turn our attention to the benefits of our 3D simulation in enabling the extraction of spatial information on optical and electronic parameters. Shown in Fig. 3 are the power flows in the α-Si:H PSCs (GaAs PSCs show qualitatively same behaviour) working in the photocurrent loss [λ = 350 nm, Figs. 3(a1) and 3(a2)] and gain [λ = 500 nm, Figs. 3(b1) – 3(b3)] regions, respectively. The images shown in Fig. 3(b3) correspond to the various z

#145911 - $15.00 USD Received 13 Apr 2011; revised 11 May 2011; accepted 13 May 2011; published 30 Jun 2011

positions shown in Fig. 3(b1). The figure clearly shows that the uniform distribution in the *xy* plane and exponential decay along the *z* direction in a conventional non-plasmonic SC have been strongly modified due to the presence of plasmonic nanostructures. Power confined in the active layers can be either decreased under short-wavelength incidence [see Figs. 3(a1) and 3(a2)] or increased under long-wavelength incidence [see Figs. 3(b1) – 3(b3)]. In the photocurrent gain region, the incident light can undergo strong forward scattering and confinement in the photoactive regions. This is especially beneficial to increase the effective optical absorption length so that photocurrent can be generated more efficiently.

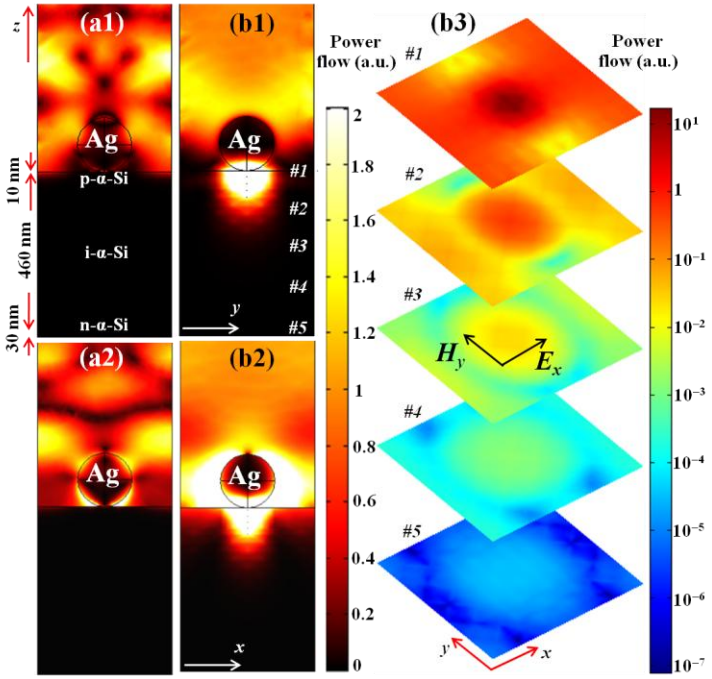

Fig. 3. Power flow distributions in the plasmonic α-Si:H SCs with 160nm-diameter silver nanoparticles decorated above. In (a1) and (a2), λ = 350 nm (in photocurrent loss region) and in (b1), (b2), and (b3) λ = 500 nm (in photocurrent gain region). In (b3), field polarizations are also given.

Figure 4 illustrates the calculated distributions of carrier generation rate and electron and hole concentrations inside the active layers of α-Si:H SCs working at λ = 500 nm [in the region of photocurrent gain as shown in Fig. 2(b)]. It is clear that the spatially modulated incident wave shown in Fig. 3 reshapes the carrier generation profile as well as modifies the carrier concentration distribution. However, the *overall* carrier concentration profiles are not significantly changed after solar injection (not shown here). This is firstly because the photo-generated carrier concentration under one-sun illumination is far less than the background; secondly, the spatial non-uniformity will be alleviated with carrier transporting inside the active layers.

The transverse dependence of the stabilized carrier profiles arising from the plasmonic nanostructures can be best seen on a logarithmic scale, as shown by Figs. 4(b1) – 4(c2). In addition, spatial information of other electronic properties (*e.g.* electrostatic potential, electrostatic field, carrier recombination rate, *etc.*) can also be obtained from our simulation. Here, we would like to emphasize that the ability to obtain detailed carrier concentration distributions inside the device is an important and experimentally accessible value. For example, a terahertz near-field microscopy technique was recently reported [37], where the authors demonstrated that the technique is capable of measuring carrier densities close to the surface of a material. They showed that regions with metals or highly conductive

#145911 - $15.00 USD Received 13 Apr 2011; revised 11 May 2011; accepted 13 May 2011; published 30 Jun 2011

semiconductors appear brightest in the THz image while semiconductors with low doping levels appear darker. Our model can provide a powerful theoretical tool to aid interpretation or corroborate the results of the terahertz near-field microscopy technique. Our model is also able to calculate the 3D carrier distribution throughout the materials, not just at the surface but internally. Since carrier recombination proceeds via different channels as various powers of carrier density, it is critical to account for local variation in carrier density to accurately predict photovoltaic device performance.

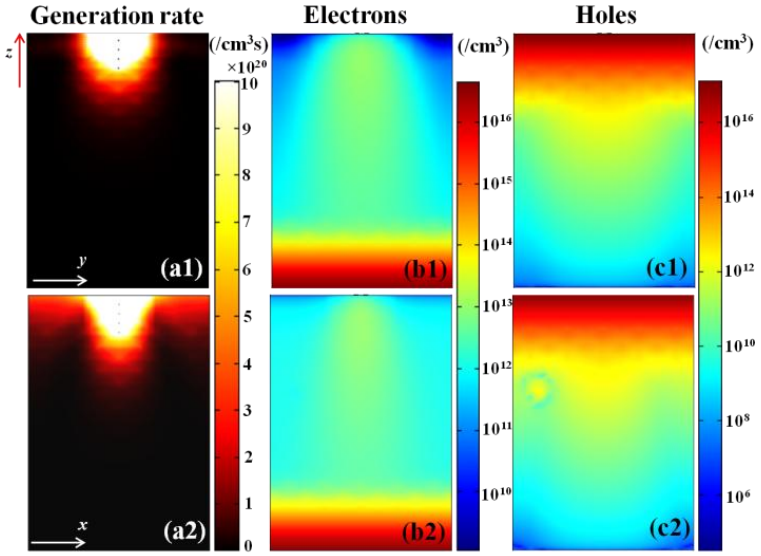

Fig. 4. Distributions of carrier generation rate [(a1) & (a2)], electron concentration [(b1) & (b2)], and hole concentration [(c1) & (c2)] inside the active layers of α-Si:H PSCs working at λ = 500 nm (in photocurrent gain region). Active layer configuration has been shown in Figs. 1(b) and 3(a1).

4. Conclusion

In summary, PSCs have been simulated using our 3D model, which calculates both the optical and electronic responses of a solar cell structure. Besides the extensively investigated optical properties, it also provides 1) a realistic measurement of the electronic performance enhancements arising from the presence of metallic nanoparticles and 2) spatial distributions of electronic parameters inside the device. Comparison between complete device simulation and optical estimation shows that carrier transport needs to be considered in a realistic SC model. Typical findings agreeing with PSC experiments and performance improvement with the incorporation of plasmonic design are verified. Since this model limits neither plasmonic nanostructure geometry nor SC configuration, it can be widely applied for the modelling of PSCs and conventional non-plasmonic SCs in 3D. Minor modifications to the model would enable light-emitting diodes and photodetectors to be modelled in a similar way.

Acknowledgments

This work was supported by EU FP7 project “PRIMA” - 248154.

#145911 - $15.00 USD Received 13 Apr 2011; revised 11 May 2011; accepted 13 May 2011; published 30 Jun 2011